Journal of Power Sources 196 (2011) 412–427

Contents lists available at ScienceDirect

Journal of Power Sources

journal homepage: www.elsevier.com/locate/jpowsour

Analysis of pulse and relaxation behavior in lithium-ion batteries

Dawn M. Bernardi[a,*], Joo-Young Go[b]

[a] Ford Motor Company, Research and Innovation Center, Dearborn, MI 48124, USA
[b] SB LiMotive, R&D team, 428-5, Gongse-dong, Giheung-gu, Yongin-si, Gyeonggi-do 446-577, South Korea

ARTICLE INFO

Article history:
Received 8 June 2010
Received in revised form 28 June 2010
Accepted 30 June 2010
Available online 8 July 2010

Keywords:
Mathematical modeling
Batteries
Hybrid electric vehicles
Lithium ion
Graphite phase behavior
Voltage relaxation

ABSTRACT

A mathematical model of a lithium-ion cell is used to analyze pulse and relaxation behavior in cells designed for hybrid-electric-vehicle propulsion. Predictions of cell voltage show good agreement with experimental results. Model results indicate the ohmic voltage loss in the positive electrode is the dominant contributor to cell overvoltage in the first instances of a pulse. The concentration overvoltage associated with the reduced lithium in the solid phase of the positive is of secondary importance through pulse duration, but dominates after current interruption. Effects of anisotropy in the particle diffusion coefficient are also studied. Heaviside mollification functions are utilized to describe the thermodynamic open-circuit voltage of lithiated graphite, and the "pleated-layer model" is extended to realize the phase behavior of primary-particle aggregates during cell operation. The negative electrode contributes little to the cell overvoltage, and two-phase behavior results in a reaction front within the electrode. No voltage relaxation is associated with the negative electrode, and after full relaxation, a stable composition gradient of lithium exists throughout the solid phase. Internal galvanic coupling removes the composition gradients in the positive electrode during relaxation.

1. Introduction

Lithium-ion batteries are currently used in a variety of portable devices such as laptop computers, cell phones, and power tools. The hybrid-electric vehicle (HEV) is the next frontier for the lithium-ion battery; the nickel-metal/hydride battery will likely be replaced by the lithium-ion battery in this application due to higher energy density, higher power density, and potential cost saving. To the user, all these advantages translate to better fuel economy at lower vehicle cost. The HEV manufacturers need a complete understanding of battery life and performance characteristics in order to design inexpensive, fuel-efficient HEVs. The purpose of this work is to develop a mathematical model of the cell from our theoretical and experimental knowledge base in order to help achieve this understanding. Mathematical models are important in all stages of product development from cell design to vehicle systems integration, fuel-economy prediction, and control-strategy design. Models can also implicate life-limiting mechanisms that ultimately affect warranty costs.

The active materials of both the positive and negative electrodes of the lithium-ion cell are lithium intercalation compounds; that is, they both can "host" lithium. The cell voltage results from the difference in the activity of lithium in the two intercalation compounds. Fuller et al. [1] published the first mathematical model of the lithium-ion cell, and we refer the reader to this work for a brief review of the cell's inception and historical makeup. These authors use the method of superposition to simulate the transport of lithium into and out-of the particles of active material that make up the electrodes. The advantage of this mathematically elegant approach is computational simplicity, and the disadvantage is the constraint of a constant Fickian diffusion coefficient for reduced lithium in the solid active material. Nevertheless, the basic theoretical framework given by Fuller et al. [1] has served as the foundation of this work as well as many other related works [2–9]. Because of recent computational advancements and software availability, in our work we are able to avoid the superposition approach and the limitations associated with it. In fact, our approach readily accommodates variations of any type and in any property; as part of our study, we investigate the effect of an anisotropic reduced-lithium diffusion coefficient on the predicted pulse power.

The attractive fuel efficiency of HEVs is gained primarily from the battery pack's ability to handle two events: (i) assist the engine during vehicle acceleration and (ii) store the vehicle's kinetic energy during deceleration[1] (to be used eventually in a future (i) event). Because these events are of short duration, on the order of seconds, relative to the operating time of, for example, a lap-

* Corresponding author. Tel.: +1 313 248 2030; fax: +1 313 621 0646.
E-mail address: dberna25@ford.com (D.M. Bernardi).

[1] Event (ii) is commonly referred to as *regenerative braking*.

0378-7753/$ – see front matter © 2010 Elsevier B.V. All rights reserved.
doi:10.1016/j.jpowsour.2010.06.107

Nomenclature

A_{cell}	area of the positive (both sides) that has opposing negative (m^2)
c_1	reduced-lithium concentration in AM (Li_xC_6 or $Li_y(NCA)O_2$) ($mol\,L^{-1}$)
c_2	concentration of $LiPF_6$ in the liquid solvent mixture ($mol\,L^{-1}$)
c_1^{max}	maximum reduced-lithium concentration (when x = y = 1) ($mol\,L^{-1}$)
D	diffusion coefficient of lithium species ($m^2\,s^{-1}$)
E	thermodynamic, open-circuit voltage (V)
f	molar activity coefficient
F	Faraday's constant, 96,485 $C\,mol^{-1}$
i_{loc}	current density localized at the particle-surface/liquid interface ($A\,m^{-2}$)
I	cell current density based on A_{cell} ($A\,m^{-2}$)
I	cell current (A)
k	charge-transfer rate coefficient
K_{junc}	liquid junction potential term (V)
L_i	half thickness of electrode paste, or thickness if $i = sep$ (m)
m_i	mass fraction of electrode component i
M_i	molar mass of component i ($g\,mol^{-1}$)
n_i	total moles of component i within the cell
r	radial distance variable of secondary AM particles (m)
r_p	characteristic radius of electrode particles (m)
R	Universal gas constant, 8.314 $J\,mol^{-1}\,K^{-1}$
S_a	specific interfacial active area for charge transfer ($m^2\,m^{-3}$)
t	time (s)
t_{Li+}	transference number of Li^+ species dissolved in liquid
T	absolute temperature (K)
ν	thermodynamic factor relating to electrolyte activity
x	distance variable through a cell component (m)
y	dimensionless radial distance of secondary particles of AM
x	average composition variable of Li in Li_xC_6 phases (or phase)
y	Li composition variable in $Li_yNi_zCo_kAl_wO_2$

Greek letters

α_a	transfer coefficient for anodic current
α_c	transfer coefficient for cathodic current
ε_i	volume fraction of component i
γ	exponent for tortuosity correction of porous medium
κ	ionic or electronic conductivity ($S\,m^{-1}$)
$\kappa_{i,j}$	coefficients in ionic conductivity expression Eq. (16)
ϕ	electric potential (V)
Θ	intercalation site for reduced lithium in host material
ρ_i	mass density of component i ($g\,cm^{-3}$)

Subscripts, superscripts, and acronyms

1	solid, electronically conductive phase, or AM
2	liquid, ion-conducting phase
AM	Active material
BI	binding agent
CA	conducting agent
chg	refers to charge
dsch	refers to discharge
host	host compound for Li (either $(NCA)O_2$ or C_6)
i	cell domain (or component) (*e.g.*, negative, positive, separator, LiC_6, etc.)
max	maximum amount of lithium species in host
neg	in the negative-electrode cell component, or in Li_xC_6 phase
NCA	acroymn for $Li_y(NCA)O_2$
o	initial or equilibrated state
p	secondary active-material particle
pos	in the positive-electrode cell component, or in $Li_y(NCA)O_2$ phase
paste	referring to the dry mixture of AM, BI, and CA pasted on the foil substrate
ref	reference composition or relative to a Li/Li^+ reference electrode
stop	refers to time duration after which current will stop
SOC	at a given state of charge
z, k	metal composition coefficients in $Li_yNi_zCo_kAl_{1-z-k}O_2$

top computer, which is on the order of hours, HEV batteries are inherently different from laptop batteries. HEV, or "power," batteries deliver their energy on short time scales, and laptop, or "energy" batteries deliver energy on long time scales. In a given volume of a cylindrically wound design, a power battery would have less active material (*i.e.*, thinner paste) and more current collecting foil (*e.g.*, more windings) than an energy battery. Accepting or delivering given amperage would initially occur at a higher voltage in the power battery than the energy battery because the current density is lower in the power battery; however, the power battery will only be able to sustain this voltage for a relatively short time. The voltage relaxation behavior of power batteries is also an important aspect for study because the behavior can have significant implications in HEV electrical systems design. Lithium-ion cells designed for energy have received more attention [1–6,10] than those designed for power. Theoretical studies in conjunction with experimental HEV-battery pulse power behavior are not readily found in the literature. Smith and Wang [8] have published such a study; however, reliable model input data were not available to them due to the cell manufacturer's proprietary interests. In our work here, the experimental cell was specifically designed as a power cell and built for comparisons with model calculations, and therefore, input data were readily obtainable.

We focus on the relatively high-voltage couple

$$Li_xC_6|Li_yNi_zCo_kAl_{1-z-k}O_2$$

in which the negative[2] is graphite and the positive[2] is commonly called "NCA," referring to the first letters of the Ni, Co, and Al that constitute the lithiated transition-metal oxide compound (abbreviated $Li_y(NCA)O_2$ henceforth).[3] A schematic description of a unit cell composed of three domains (*i.e.*, L_{neg}, L_{sep}, and L_{pos}) within a cell stack or spiral is shown in Fig. 1. Albertus et al. [11] have modeled NCA as a component of mixed positive active materials in coin cells with a lithium metal negative. More recently Dees et al. [12] report a study of HEV cells. We also present a new detailed treatment of lithiated graphite that interprets the phase behavior and its effects on negative-electrode utilization.

[2] We refer to the negative electrode as the "negative" and the positive electrode as the "positive".

[3] Composition coefficients z and k for this particular transition-metal NCA compound are proprietary.

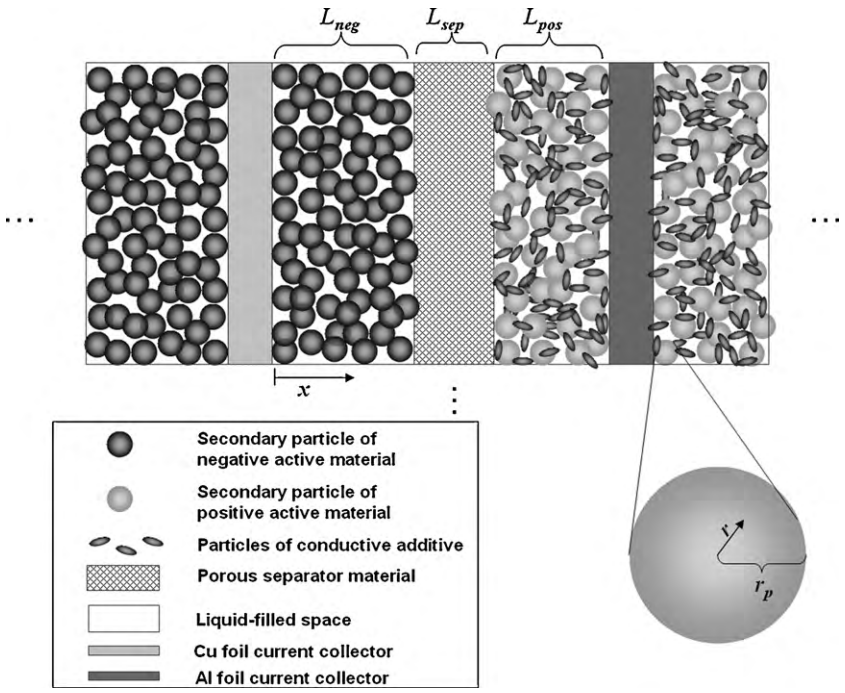

Fig. 1. Diagram of a separator sandwiched between two pasted foil electrodes (three dots indicate repetition or length). We show the two dimensions "x" and "$y = r/r_p$" in which the model equations are solved. The unit cell is shown to consist of the separator and two, electrode half thicknesses.

2. Experimental

The cell employs an electrolytic solution of lithium salt dissolved in a mixture of organic carbonate solvents and a 30-μm polypropylene separator. The cell was the cylindrically wound type and of small size in order to minimize thermal excursions. The active area was approximately 192.5 cm^2, which is the total electrode active area based on both sides of the pasted, positive, foil current collector used. (Current density would be based on this active area.) The pasted current-collecting substrates consisted of 3 or 4 layers of particles of active material (AM) mixed with binder (BI) and conducting agent (CA). Battery fabricators typically give an "N/P ratio" for a particular cell design from specific capacities given by the materials supplier, area-specific paste densities, and mass fractions. For an example case of a 372 mA g^{-1} specific capacity (based on graphite mass), an 81.3% paste graphite mass fraction, and an area-specific paste density of 10 mg cm^{-2}, one would calculate the area-specific capacity of the negative to be 3.02 mAh cm^{-2}. The area-specific capacities for the positive and negative materials of our experimental cell are 2.13 and 3.02 mAh cm^{-2}, respectively,[4] which results in an N/P ratio of 1.42 for this cell.

The cell was conditioned by cycling three times at ambient conditions, starting with charge, before the pulse tests. This constant-current cycling was at 230 mA to a 4.2-V charge limit and approximate 2.8-V discharge limit with a 1-h rest in between. On the second and third discharges the cell delivered 197.8 mAh of capacity. We take this capacity as a reference and define state-of-charge (SOC) as the percent of this value and the "C-rate" of discharge as 197.8 mA. The open-circuit voltage (OCV) of the cell after each of the three conditioning charges was 4.1797, 4.181, and 4.167, respectively. The pulse tests were performed at 65% and 35% SOC. The initial SOC was set by a 1-C rate discharge 1 h after full charge for the appropriate time; 1260 s (= $(1 - 0.65) \times 1$ h) for 65% SOC, for example. One hour after setting the cell SOC the open-circuit cell voltage was stable and considered to be characteristic of the particular SOC: 3.8264 and 3.6680 V, respectively for 65% and 35% SOC.

Pulse tests followed the previously described conditioning tests. Each constant-current 40 s pulse was followed by a 5 m rest with data recorded at 0.2-s intervals during this 340 s event. After each pulse test the cell was returned to the original SOC by first returning the amount of charge (in A s) at the 1-C rate followed by a constant voltage charge at the characteristic OCV. Charge was terminated when the current declined to C/20. Three discharge pulse tests at rates of 3C, 5C, and 10C were followed by charge pulse tests at the same rates.

3. Theoretical

The basic reaction

$$\Theta + Li^+ + e^- \leftrightarrows \Theta\text{–}Li \quad (1)$$

represents the electrochemical insertion/extraction of lithium in the host electrode materials during cell operation. The model was constructed within the Chemical Engineering Module of the COMSOL Multiphysics® software environment (Version 3.4) [13]. The basic equations for a model of the Graphite|Li(NCA)O_2 system would be similar to those for the Coke-carbon|$LiMn_2O_4$ system, which are described as an example the Comsol Multiphysics® user's guide for Version 3.5a [14]. The COMSOL example is based on the on the work of Doyle et al. [15,16].

Section 3.1 gives the four non-linear coupled partial differential equations (Eqs. (2)–(5)) that correspond to the model's four dependent variables ϕ_1, ϕ_2, c_1, and c_2. The three independent variables are two distance variables, x and r, and time, t. All other quantities in these four main equations are functions of the dependent variables (given in Section 3.2) or constants (given in Section 3.3). In Section 3.4 we describe our model of insertion and extraction of Li in graphite. Section 3.5 gives the parameters for the heaviside-type functions used in the model to describe the step-change behavior

[4] Note that graphite's intercalation maximum has been established to be 372 mA g^{-1} (based on mass of graphite) [18].

of the voltage plateaus of lithiated graphite and current during cell operation.

3.1. Model equations

The first equation is related to current conservation and Ohm's law for the electronically conducting solid phase (denoted by subscript 1)

$$\nabla \cdot \left(-\frac{\kappa_1^{eff}}{L_i} \nabla \phi_1 \right) = -i_{loc} S_{a,i} L_i \tag{2}$$

where the differentiation operator is with respect to a dimensionless distance variable x/L_i. The next equation is current conservation and a form of Ohm's law for the ion-conducting liquid phase (denoted by subscript 2)

$$\nabla \cdot \left[-\frac{\kappa_2^{eff}}{L_i} \left(\nabla \phi_2 - \frac{K_{junc}}{c_2} \nabla c_2 \right) \right] = -i_{loc} S_{a,i} L_i \tag{3}$$

Eqs. (2) and (3) are entered in the "PDE, General Form" application mode of the software for each cell domain *i*. Because there is no solid electron-conducting phase in the separator domain, Eq. (2) applies only in the electrode domains. The third equation represents a material balance on the salt $LiPF_6$ dissolved in the liquid phase:

$$\varepsilon_{2,i} L_i \frac{\partial c_2}{\partial t} + \nabla \cdot \left(-\frac{D_2^{eff}}{L_i} \nabla c_2 \right) = i_{loc} S_{a,i} L_i \frac{1 - t_{Li^+}}{F} \tag{4}$$

This equation is entered in the "Diffusion" application mode of software's Chemical Engineering Module and applies in the separator and both electrode domains. In the fourth equation we introduce a second dimension, *r*, as the distance from the center of the spherical secondary particles that exist throughout the electrodes. We define a dimensionless distance variable for each electrode: $y = r/r_p$, scaled by the particle radii in each electrode. In terms of *y*, Fick's law in spherical coordinates can be written as

$$y^2 r_p \frac{\partial c_1}{\partial t} + \nabla \cdot (-\mathbf{D}_1 \nabla c_1) = 0 \tag{5}$$

where $\mathbf{D}_1$ is a tensor that is entered in the software package that characterizes solid-state diffusion of the reduced-lithium species within (in the *y* direction), but not between particles (in the *x* direction of each electrode)

$$\mathbf{D}_1 = \begin{bmatrix} \dfrac{y^2 D_1 \times 10^{-6}}{r_p} & 0 \\ 0 & \dfrac{y^2 D_1}{r_p} \end{bmatrix} \tag{6}$$

This assumption is appropriate for electrodes with relatively low particle packing density. The matrix is meant to characterize anisotropic diffusion in a two-dimensional system with components *xx*, *xy*, *yx*, and *yy*, reading left to right. The 10^{-6} factor in the *xx* component reflects the suppression of particle-to-particle diffusion. Eq. (5) is entered for the second dimension in the "Diffusion" application mode of software's Chemical Engineering Module and applies in both electrode domains [14].

There are four boundaries in the unit cell of three domains; the boundaries labeled 1 through 4, respectively, are the negative/current-collector, negative/separator, positive/separator, and positive/current-collector interfaces. The interfacial conditions are entered in menu format and are described in the following. The potential ϕ_1 is arbitrarily set to zero at boundary 1. At boundary 4, I_{dsch} is specified and is characterized by a heaviside-type function given in Section 3.5. The flux of liquid species is set to zero at both boundaries 1 and 4. Liquid species flux, species concentration, and ϕ_2 are taken to be continuous at boundaries 2 and 3. The two distance dimensions are linked by the constraint that the flux of lithium at $y = 1$ is determined by i_{loc} (see Eq. (9)). The symmetry (insulating) condition on the flux of reduced-lithium species applies at the centers of the particles ($y = 0$).

3.2. Functions of the dependent variables

The quantities that will be described here are functions of one or more of the four dependent variables ϕ_1, ϕ_2, c_1, and c_2 in Eqs. (2)–(5). These quantities are i_{loc}, E_{ref}^{neg}, v, κ_2, and D_2. The solid diffusion coefficient D_1 could also be assigned a functional dependence on c_1 in the same manner. Data points (see Fig. 4) for the "Interpolation Function" E_{ref}^{pos} are read from an external file.

Bruggeman-type relations [19]

$$\kappa_1^{eff} = \kappa_1 \varepsilon_1^{\gamma_1}, \qquad \kappa_2^{eff} = \kappa_2 \varepsilon_2^{\gamma_2}, \quad \text{and} \quad D_2^{eff} = D_2 \varepsilon_2^{\gamma_2} \tag{7}$$

are used to account for the effect of the porous media on the transport properties that are given in the following subsections. Because the two kinetic parameters S_a (Eqs. (2)–(4)) and *k* (see Eqs. (9) and (10)) always exist as a product, they are not independent. We do, however, use the expression in each electrode

$$S_a = \frac{3\varepsilon_1}{r_p} \tag{8}$$

which describes the specific surface for isolated spheres.

3.2.1. Local current density

Eqs. (2)–(4) and the boundary conditions involve the local current density at the solid/liquid interface within the pores of the electrodes. For the positive electrode we use

$$i_{loc} = k_{pos} c_1^{\alpha_c,pos} c_2^{\alpha_a,pos} (c_{1,pos}^{\max} - c_1)^{\alpha_a,pos} \times \left[\exp\left(\frac{\alpha_{a,pos} F}{RT} (\phi_1 - \phi_2 - E_{ref}^{pos}) \right) - \exp\left(-\frac{\alpha_{c,pos} F}{RT} (\phi_1 - \phi_2 - E_{ref}^{pos}) \right) \right] \tag{9}$$

The equivalent of Eq. (9) is utilized in Ref. [15]. For the negative electrode we use

$$i_{loc} = k_{neg} c_2^{\alpha_a,neg} \left[\exp\left(\frac{\alpha_{a,neg} F}{RT} (\phi_1 - \phi_2 - E_{ref}^{neg}) \right) - \exp\left(-\frac{\alpha_{c,neg} F}{RT} (\phi_1 - \phi_2 - E_{ref}^{neg}) \right) \right] \tag{10}$$

We elected to exclude solid-phase concentration terms in Eq. (10) that would reflect composition dependence of the exchange-current density because of the following; for the conditions in this study, the intercalated graphite is in a two-phase region and we expect lithium insertion and extraction to occur at the LiC_{12}/liquid interface (see Section 3.4). In contrast, the local composition of the $Li_y(NCA)O_2$ varies and warrants the composition dependency in Eq. (9).

3.2.2. Liquid junction and electrolyte activity

Eq. (3) includes the liquid-junction potential [27], which is reflected in the expression

$$K_{junc} = \frac{2RT}{F} \left[1 + \left(\frac{v}{(1 - t_{Li^+})} - 1 \right) \right] (1 - t_{Li^+}) = \frac{v 2RT}{F} \tag{11}$$

where the equation[5]

$$v = 0.601 - 0.24c_2^{1/2} + 0.982\,[1 - 0.0052(T - 294)]\,c_2^{3/2} \quad (12)$$

fits data reported in Ref. [17] (0 to 4 M $LiPF_6$ from 263 to 333 K). Even though the carbonate solvent mixture is somewhat different than that used in our experimental cell, we assume that Eq. (12) applies in our system. The quantity v is related to the electrolyte activity coefficient by the expression

$$v = (1 - t_{Li^+})\left(1 + \frac{d\ \ln f}{d\ln c_2}\right) \quad (13)$$

3.2.3. Electrolyte diffusion coefficient

The temperature and concentration dependence of the diffusion coefficient of $LiPF_6$ is fit by the equation[5]

$$\log_{10} D_2 = -4.43 - \frac{54}{T - (229 + 5c_2)} - 0.22c_2 \quad (14)$$

in Ref. [17] (0 to 4 M $LiPF_6$ from 263 to 333 K). Again, we use this equation in our calculations even though our solvent mixture is different than that used in [17]. Data given in this reference indicate that the transport properties of $LiPF_6$ in carbonate solvents are strong functions of c_2 and T and much weaker functions of the specific carbonate solvent mixture.

3.2.4. Liquid-phase ionic conductivity

In contrast to v and D_2, we made some of our own measurements of the ionic conductivity of the liquid phase, κ_2. We used an expression of the form [17]

$$\sqrt{\frac{\kappa_2(c_2, T)}{c_2}} = \sum_{i=0}^{n}\sum_{j=0}^{k}\kappa_{i,j}c_2^i T^j \quad (15)$$

The $\kappa_{i,j}$ coefficients were determined by using standard parameter-estimation methods with experimental data in the intermediate range of concentrations and data from [17]. The measured data were thirty ionic conductivity measurements for the solvent ethylene carbonate/ethyl-methyl carbonate/di-methyl carbonate (30:40:30, vol%) at 253, 273, 293, 313 and 333 K in the concentration range of 0.8 to 1.4 M $LiPF_6$. We also used five conductivity values from Ref. [17]: values at 4 M $LiPF_6$ for each of the five above temperatures. These five values were calculated from Eq. (15) using the $\kappa_{i,j}$ coefficients for a different solvent (propylene carbonate/ethylene carbonate/di-methyl carbonate, 10:27:63, vol%). We did this because our investigations indicated that data at high concentration are required in order to obtain the experimentally observed behavior of $\kappa_2 \to 0$ as $c_2 \to \infty$ [17]. Eq. (15) with $n = k = 2$ can be written as[5]

$$\sqrt{\frac{\kappa_2(c_2, T)}{c_2}} = \kappa_{0,0} + \kappa_{0,1}T + \kappa_{0,2}T^2 + \kappa_{1,0}c_2 + \kappa_{1,1}c_2T + \kappa_{1,2}c_2T^2 + \kappa_{2,0}c_2^2 + \kappa_{2,1}c_2^2T \quad (16)$$

The MATLAB® parameter-estimation function *nlinfit* was used to obtain the nine $\kappa_{i,j}$ coefficients given in Table 1 from the 35 κ_2 values discussed above. (Note that the values of c_2 and T in this expression should be in units of mol L^{-1} and Kelvin, respectively, and the expression results in units of mS cm^{-1} for κ_2.)

The continuous lines in Fig. 2 give κ as a function of c_2 according to Eq. (16) with the $\kappa_{i,j}$ coefficients given in Table 2 for various temperatures. The symbols in this figure show the 35 experimental data points used to get the $\kappa_{i,j}$ coefficients. We would like to comment on the comparison of the κ_2 data reported in [17] with the solvents propylene, ethylene, and di-methyl carbonate to data reported here with a different carbonate mixture. For temperature at or above 293 K, the maximum κ_2 values in [17] occurred at lower c_2 values (~1.0 M at 293 K) than those shown in Fig. 2 (~1.25 M at 293 K). At 273 K the maxima appeared to coincide. In general, the values in [17] were lower by 5–7%, with the smaller difference being at the lower temperatures (<293 K). One might expect similar differences in v and D_2 relating to the solvent mix.

Table 1
The coefficients, $\kappa_{i,j}$, for Eq. (16) found to represent the experimental κ data.

$\kappa_{i,j}$	$j=0$	$j=1$	$j=2$
$i=0$	−8.2488	0.053248	−0.000029871
$i=1$	0.26235	−0.0093063	0.0000080690
$i=2$	0.22002	−0.00017650	0.0000

3.2.5. Thermodynamic open-circuit voltage

The expressions for E_{ref}^{pos} and E_{ref}^{neg} in Eqs. (9) and (10), respectively, are both functions of c_1, however, here we utilize the composition variables x and y. Because we are neglecting density variations, c_1 in the positive and negative, respectively, relates to x and y through

$$x = \frac{c_1}{c_{1,neg}^{max}} \quad \text{and} \quad y = \frac{c_1}{c_{1,pos}^{max}} \quad (17)$$

The relations $E_{ref}^{neg}(x)$, and $E_{ref}^{pos}(y)$ were obtained through our own independent investigations and are given in Figs. 3 and 4, respectively. The E_{ref}^{pos} data were obtained from a C/24-rate discharge of a coin-sized piece of electrode material *vs.* a Li counter electrode. We chose the composition scale shown, $0.3 < y < 1$, because experimental OCV data agreed most favorably with these data and our estimate of n_{NCA} (see Table 2). Also shown in Fig. 4 are voltages from a second data set superimposed on this scale. The C/24 data consist of 254 points in the range of 3–4.28 V. Linear interpolation mode was used in the model to represent the $E_{ref}^{pos}(y)$ function.

The second data set was used for $y < 0.4$ because these data more accurately described the experimental OCV data observed after the charge pulses. Our supposition of $0.3 < y < 1$ corresponds to a

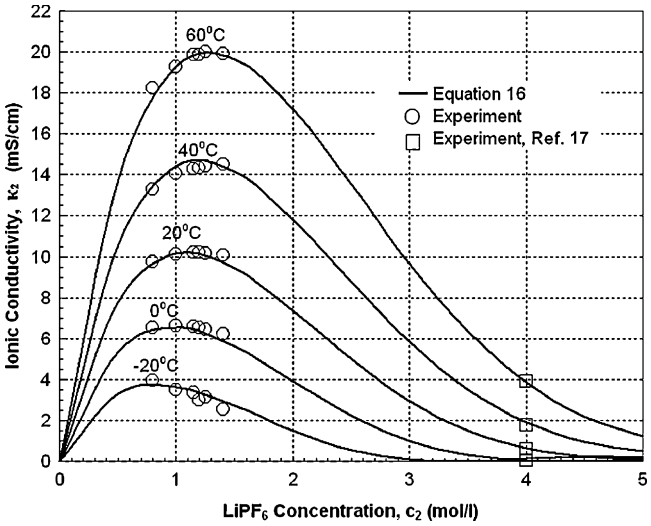

Fig. 2. Ionic conductivity of the liquid electrolytic solution as a function of salt concentration and temperature. The solid line represents the results of Eq. (16) and the symbols represent experimental measurements.

[5] Note that the values of c_2 and T in this expression should be in units of mol L^{-1} and Kelvin, respectively, and the expression for D_2 results in units of $cm^2\ s^{-1}$.

Table 2
Model base-case electrode constants.

Quantity	Positive electrode	Negative electrode
Total moles of active host material, n_{host} (mol)	1.218×10^{-2}	1.154×10^{-2}
Volume fraction of active material, $\varepsilon_1 = \varepsilon_{AM}$	0.4676	0.5802
Volume fraction of liquid phase, ε_2	0.3382	0.3825
Volume fraction of conductive agent, ε_{CA}	0.0982	0
Volume fraction of binder, ε_{BI}	0.0960	0.0383
Electronic conductivity of [29] AM, κ_1 (S m^{-1})	0.04	16,700
Lithium diffusion coefficient in AM, D_1 (m^2 s^{-1})	0.14×10^{-13}	1×10^{-13}
Exponent for κ_1 tortuosity correction, γ_1	1.5	1.5
Charge-transfer rate coefficient, k [A m^{-2}(m^3 mol^{-1})$^{2/3}$]	2.3×10^{-3}	7.5×10^{-4}
Anodic transfer coefficient, α_a	0.5	0.5
Cathodic transfer coefficient, α_c	0.5	0.5
Molar density of AM for x = y = 1, c_1^{max} (mol Li m^{-3})	49,195	28,200
Initial composition of AM, $x^0_{65\%}$ and $y^0_{65\%}$	0.5173	0.7691

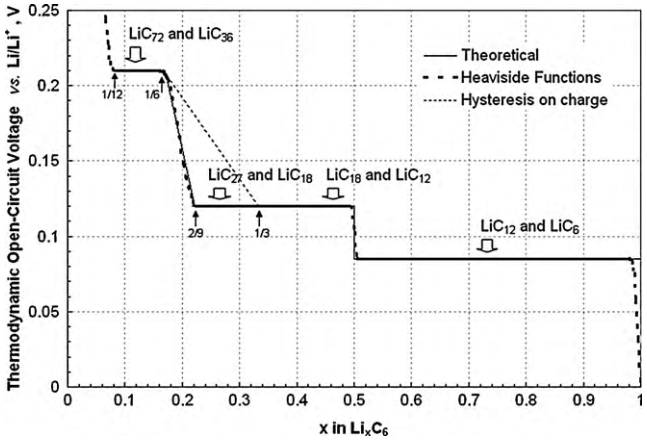

Fig. 3. Thermodynamic open-circuit voltage behavior of graphite as a function of degree of lithiation. The compositions noted and voltage plateaus are based on the work of Ohzuku et al. [18] and are designated by the solid line. The dotted line is the hysteresis observed by Ohzuku upon lithiation. The dashed line is the heaviside-function approximation used for $E^{neg}_{ref}(x)$.

theoretical maximum capacity of 195 mAh g^{-1} (based on mass of Li(NCA)O_2). The solid line in Fig. 3 is theoretical and based on the compositions of equilibrated phases and three corresponding voltage plateaus identified by Ohzuku et al. [18] and is discussed in greater detail in Section 3.4.

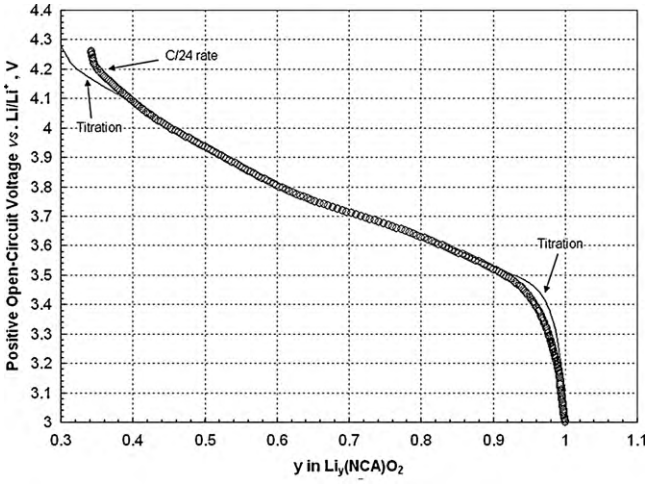

Fig. 4. Open-circuit voltage behavior (*vs.* a lithium reference) of the positive electrode as a function of degree of lithiation. The open circles are the results of a discharge that is 24 times lower than the C-rate. These data are used to represent $E^{pos}_{ref}(y)$ in the model for y > 0.36.

Table 3
Base-case operating conditions and separator properties.

Cell 1C current, I	0.1978 A
Positive area (both sides) with opposing negative, A_{cell}	0.01925 m^2
Cell pulse discharge current density, I_{dsch} (5C rate)	51.37 A m^{-2}
Discharge pulse duration, t^{stop}_{dsch}	40 s
Open-circuit rest period, t_{ocp}	300 s
Cell temperature, T	298 K
Initial $LiPF_6$ concentration in liquid phase, c_2^0	1150 mol m^{-3}
Transference number of Li^+ in liquid, t_{Li+}	0.38[17]
Separator thickness, L_{sep}	30×10^{-6} m
Volume fraction of liquid within separator, ε_2^{sep}	0.46
Exponent for D_2 and κ_2 tortuosity correction, γ_2	1.5

3.3. Model constants

Eqs. (2)–(17) constitute all the model relationships, with their associated constants. Since our objective was to adjust minimal input items to fit the experimental voltage response, the constants were mostly obtained from literature references, design specifications, and experimental operating conditions. For example, particle sizes and electrode thicknesses were measured and correspond to model input values of r_p, L_{pos}, and L_{neg}, however, we can not disclose the actual values due to the proprietary nature of the cell design. All the other model constants are given in the following tables. Table 2 gives electrode constants and Table 3 gives separator constants and operating conditions for the base-case conditions of 65% SOC. The molar density of Li(NCA)O_2 in Table 2 was obtained from our crystallographic measurements (a = 2.865 Å, c = 14.185 Å). The molar density of LiC_6 given in the table was extracted from the graphene layer spacing reported by Ohzuku et al. [18] The Li host compound is (NCA)O_2 (denoted by subscript NCA) for the positive[6] and C_6 for the negative, and we define the total moles of active host n_{host} in an electrode at assembly as

$$n_{NCA} = \frac{A_{cell} L_{pos} m_{NCA} \rho_{paste}}{M_{NCA}} \quad \text{and} \quad n_{C_6} = \frac{A_{cell} L_{neg} m_{C_6} \rho_{paste}}{M_{C_6}} \qquad (18)$$

for the positive and negative electrodes, respectively. The total moles of graphite and Li(NCA)O_2 (x = 0 and y = 1) upon assembly give the values of n_{host} in Table 2. In the model, however, we take only the pasted material associated with the overlap area of the positive and negative to be utilized; values of n_{host} in Table 2 are based on A_{cell} rather than true electrode pasted areas.

The volume fractions of paste components at cell assembly can be obtained from

$$\varepsilon_i = \frac{m_i \rho_{paste}}{\rho_i} \quad i = \text{CA, BI, Li(NCA)}O_2\text{, or } C_6 \qquad (19)$$

[6] Note that the moles of the pasted active material Li(NCA)O_2 is the same as the moles of host.

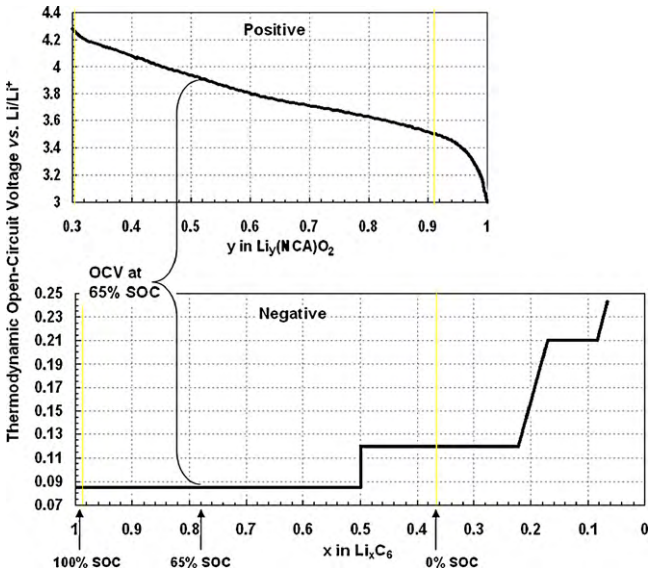

Fig. 5. Thermodynamic open-circuit voltage of the positive and negative relative to a lithium reference (from Figs. 3 and 4) with the composition axis adjusted to correspond to SOC.

Because in our model we take the density of $Li_y(NCA)O_2$ to be independent of "y," we can use the relation $\rho_{NCA} = c_{1,pos}^{max} M_{NCA}$. The value from Eq. (19) for y = 1 is therefore used to represent the volume fraction of $Li(NCA)O_2$ at conditions near 65% SOC and given in Table 2. For the negative, the value obtained from Eq. (19) should be converted from C_6 to a value corresponding to lithiated graphite material at 65% SOC. We assume a molar density of $0.0300\,(\mathrm{mol\,C_6})\,\mathrm{cm}^{-3}$ for the mix of lithiated graphite at this SOC. The molar density of C_6 is $0.0312\,(\mathrm{mol\,C_6})\,\mathrm{cm}^{-3}$. The volume fraction of lithiated graphite was obtained by multiplying ε from Eq. (19) by the ratio 0.0300/0.0312. This method implies that an increase in solid volume will correspond to a loss of void volume rather than in increase in total volume, which is a likely scenario for a cell under compression. We also assume that all the void volume calculated using Eq. (19) is filled with the liquid electrolytic solution. Separator thickness and porosity are based on manufacturer's specifications. Standard Bruggemann [19] corrections for tortuosity are employed, and transfer coefficients are in accordance with the work of Verbrugge and Koch [20].

The solid phase diffusion coefficient of lithium, D_1, should be a function of c_1 [21,22]; however, c_1 variations are relatively small due to the short pulses near a given SOC that are investigated in this work. At least for our work, this suggests the validity of using a single D_1 and also supports constancy in other model parameters, such as density, that may in actuality be functions of c_1. Because model results are very sensitive to D_1 in the positive, D_1^{pos} was adjusted to obtain a good fit to all the experimental data. No other parameters were taken as adjustable. Details of the fitting and sensitivities are given in Section 4.

3.3.1. Initial active-material compositions

Here we detail the way in which we obtained the last entry in Table 2. Fig. 5 shows the data of Figs. 3 and 4 with the abscissae adjusted so that $x^0_{65\%}$ and $y^0_{65\%}$ from Table 2 coincide, and $E_{cell}(x, y)$ can be seen as the difference $E_{ref}^{pos}(y) - E_{ref}^{neg}(x)$. The value of the model input parameter $x^0_{65\%}$ was obtained from an estimate of the OCV at 65% SOC. We made this estimate by taking the average of the OCV values measured before each of the three discharge pulses, which resulted in 3.825 V. Then we made the assumption that $1 > x^0_{65\%} > 1/2$, which is reasonable because we expect a fresh cell at 65% SOC to be on the negative's 85-mV plateau. This allows us to calculate $E_{ref}^{pos}(y)$, and therefore $x^0_{65\%}$, from

$$E_{cell}(x, y) = E_{ref}^{pos}(y) - E_{ref}^{neg}(x) \tag{20}$$

since $\mathrm{OCV}(65\%) = 3.825\,\mathrm{V} = E_{cell}(x^0_{65\%}, y^0_{65\%})$ and $E_{ref}^{neg}(x^0_{65\%}) = 0.085\,\mathrm{V}$. This results in $y^0_{65\%} = 0.5175$.

The value $x^0_{65\%} = 0.7691$ in Table 2 was estimated based on the discharge pulse data at 35% SOC that evidenced the 35-mV difference (between the 85 and 120 mV plateaus) from the OCV data. With this method, the error in our estimate of $x^0_{65\%}$ could not be more than the remainder of the 85-mV plateau, which would result in $x^0_{0\%} = 0.09$ in Fig. 5.

For our case of constant current pulses, changes in active material compositions can be calculated;

$$\Delta y = \frac{It}{n_{NCA}F} \tag{21}$$

$$\Delta x = -\frac{It}{n_{C_6}F} \tag{22}$$

The value $x^0_{65\%} = 0.7691$ appears reasonable because we calculate $x^0_{100\%} = 0.9870$ from Eq. (22); in other words, we expect the negative to be dominantly LiC_6 when then the cell in the fully charged state. Fig. 5 also shows the electrode compositions corresponding to 0 and 100% SOC calculated from the above equations. (Recall that percent capacity changes are based on the cell rated capacity of 197.8 mAh.)

3.3.2. Active-material composition changes during life

Fig. 5 also illustrates the shift of the negative's composition relative to the positive's during formation because prior to formation (at assembly) y = 1 would rest directly above x = 0. Our results indicate that y = 1 rests above x = 0.3 after formation. This type of shift, as well as a change in N/P ratio, may occur as a cell's performance changes throughout life. With or without a shift, the range of compositions corresponding to 100% SOC may change throughout life as well. Temperature changes will also have effects, especially with respect to the voltages. Fig. 5 shows very fundamental cell data, and any model at the very least, would have to be able to characterize the changes to these data with life. We also want to reiterate that our modeling was not used to obtain the results shown in this figure; rather the results are a prerequisite.

3.4. Model of the graphite insertion and extraction

Based on the findings of Ohzuku et al. [18] we constructed the solid line in Fig. 3 as the thermodynamic OCV of intercalated graphite and used this as a basis for the function $E_{ref}^{neg}(x)$ in the model. Ohzuku et al. [18] identified the compositions of equilibrated phases and three corresponding voltage plateaus: 85 mV, 120 mV, and 210 mV *vs.* Li/Li^+. The solid electrolyte interphase [23,24] (SEI) that is known to exist at the solid/liquid interface is not explicitly accounted for in the model. We do, however, presume that the presence of the SEI allows us to neglect a host of reactions involving the electrolytic solution. We also assume that the SEI layer offers negligible resistance. The "pleated-layer model" [25] was the basis for our discussions of the dynamic behavior of the negative electrode and is discussed at the end of this section.

3.4.1. Thermodynamic behavior

According to the observations of Ohzuku et al. [18] reversible de-intercalation (*i.e.*, discharge) of LiC_6 ($1 > x > 0$) would proceed as follows: LiC_{12} will nucleate upon extraction of Li from pure LiC_6

Table 4
Heaviside mollification function parameters.

Function	Variable	Variable center	Variable span
I, A cm^{-2}	t, s	$t = 40$ s	0.1 s
E_{ref}^{neg} (from 0 to 85-mV plateau)	x	x = 1	0.02
E_{ref}^{neg} (85–120-mV plateau)	x	x = 0.5	0.005
E_{ref}^{neg} (120–210-mV plateau, discharge)	x	x = 0.1944	0.03571
E_{ref}^{neg} (120–210-mV plateau, charge)	x	x = 0.25	0.1
E_{ref}^{neg} (210-mV plateau to 3.7 V at x = 0)	x	0	0.08333
D_1^{pos} (anisotropic case in Section 4.4)	y	$y = 0.994$	0.002

(x = 1) and coexist on the 85-mV plateau with LiC_6 in two-phase equilibrium until x = 1/2. At this point LiC_6 will cease to exist, LiC_{18} will nucleate, and there will be a step-change in voltage to the 120-mV plateau. De-intercalation in the region 1/2 > x > 2/9 constitutes a 120-mV plateau made up of two, two-phase segments. In the first segment, 1/2 > x > 1/3, LiC_{18} coexists with LiC_{12}. At x = 1/3, LiC_{27} is formed and LiC_{12} is exhausted; in the second segment, 1/3 > x > 2/9, LiC_{18} and LiC_{27} exist in two-phase equilibrium. (Intercalation in this region 2/9 < x < 1/3 indicates hysteresis and is discussed below.) With continued de-intercalation to the point x = 2/9, only LiC_{27} exists. De-intercalation then transforms this compound as a single phase of continuously varying composition to LiC_{36} within the region 2/9 > x > 1/6. At x = 1/6, LiC_{72} nucleates and coexists with LiC_{36} in two-phase equilibrium in the region 1/6 > x > 1/12 on the 210-mV plateau. De-intercalation of LiC_{72} in the region 1/6 > x > 0 appears to be single phase and involves very large voltage excursions as pure graphite is approached. Since step changes in any model parameter normally cause significant numerical difficulties, a heaviside-type function was utilized to "round out" the transitions shown by the solid line. The small circles in Fig. 3 show the behavior of the function used for discharge (de-intercalation) in the model to represent E_{ref}^{neg}. The parameters of the function are given in Table 4, which give parameters for the other heaviside functions used in the model.

Intercalation would proceed as the reverse of what was described above with one exception due to hysteresis: the single-phase region with the endpoint x = 1/6 (where pure LiC_{36} exists) upon intercalation is wider (than the single-phase region during de-intercalation) and extends to x = 1/3. Within this region LiC_{36} is transformed as a single phase of continuously varying composition to LiC_{18}. Further intercalation would precipitate LiC_{12} as it would follow, from that point on, the reverse of the previously described thermodynamic de-intercalation process. Although the model incorporates the thermodynamic behavior of the full range of Li composition in graphite (1 > x > 0), in the discharge behavior shown in this work, we will see that x simply approaches 1/2 and the second plateau is never reached during the pulses. Discharge pulses from a lower SOC, for example from 35% SOC, would more likely terminate on this 120-mV plateau.

3.4.2. Dynamic behavior

Fig. 6 shows a schematic (top view) of intercalated lithium sitting on top of carbon hexagons in a graphene layer [25]. Repeatedly stacking this whole construct would constitute the compound LiC_6; placing an extra graphite layer between this while stacking would constitute the compound LiC_{12}.[7] The primary particles of lithiated graphite are highly ordered "stacks" which themselves would be hexagonally shaped as shown in Fig. 7a. The secondary particles are

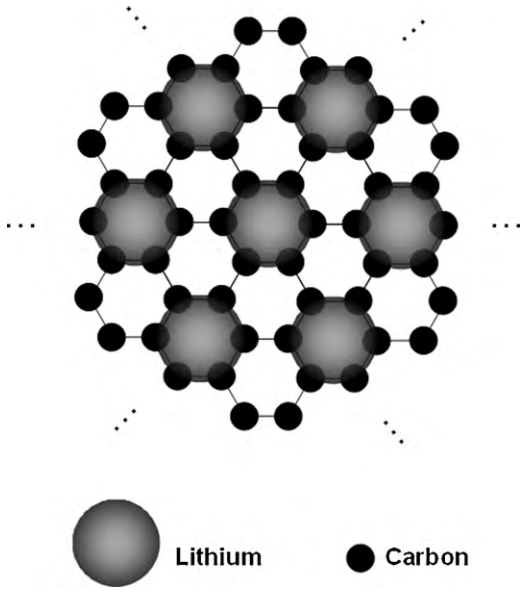

Fig. 6. Top view of a single, fully lithiated graphene plane. Each reduced-lithium species is situated on top of a carbon hexagon.

on the order of 10 μm and are comprised of many of the primary particles. A schematic of a cross section through the center of a secondary particle during discharge is shown in Fig. 7b. Fig. 8 shows a side view of LiC_6 and LiC_{12} phases in accordance with the "pleated-layer model," which describes how phase transitions occur with in-plane movement of lithium [25]. During discharge the boundary between the two phases moves rightward in one dimension as lithium is removed at the interfacial edge. The interfacial edge could be the solid/liquid interface if the primary particle were located near the surface of the secondary particle.[8] In this case, removal of lithium would be the result of the charge-transfer oxidation reaction (see Eq. (1)). For a primary particle embedded within the secondary particle, the interfacial edge would be perhaps the edge of another primary particle. Removal of lithium in this case would be the result of random motion and rearrangements. In the model we treat this as a diffusive process with the gradient of average Li concentration (see Eq. (5)) as the driving force even though the secondary particle is actually composed of the two distinct phases LiC_6 and LiC_{12}. This driving force for lithium rearrangement results in equilibrated secondary particles that exhibit no radial variation in the relative amounts of the two phases. However, equilibrated secondary particles at various positions throughout the thickness of the electrode will have differences in the relative amount of the two phases, since diffusion between secondary particles does not occur in the model. The diffusion coefficient may be more responsible for characterizing rearrangement between primary particles, rather than within them and therefore would not be an inherent property of lithiated graphite; D_1 would then likely be dependent on preparation methods, primary particle size, and other factors as well.

Fig. 7a depicts an extension of the one-dimensional pleated-layer model to a primary particle stack. Here, a fully charged primary particle would be dominantly LiC_6 and is shown at the top. Removal of lithium from interfacial edges would result in formation of LiC_{12} in the center of the stack. The phase boundary is now six planar areas that move in two dimensions toward the six, stationary planar edge areas. Transition of a primary particle from LiC_6 to LiC_{12}

[7] LiC_6 is known as a stage-1 compound; LiC_{12} a stage-2 compound. Placing yet another graphite layer between this while stacking would produce a stage-3 compound, etc.

[8] In actuality, the thin, ion-conducting SEI layer would exist between the solid AM and liquid.

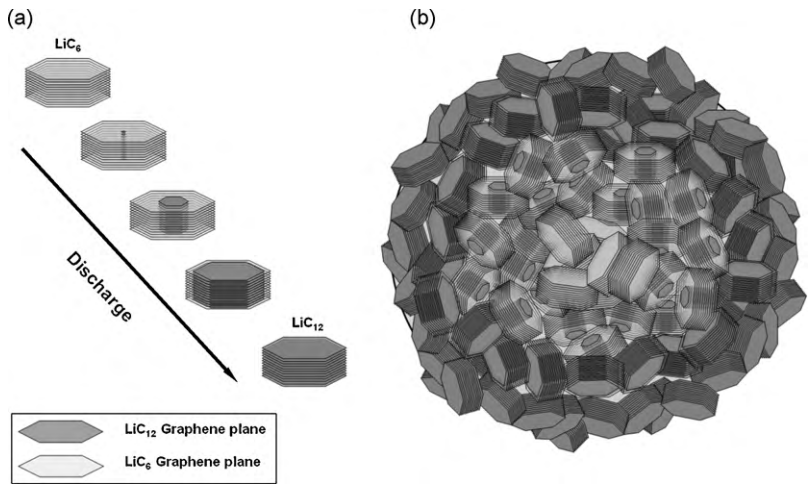

Fig. 7. Primary particles (a) of lithiated graphite at various degrees of lithiation on the 85-mV plateau during discharge. Cross section of a secondary particle (b) of lithiated graphite during dynamic discharge. The center is primarily composed of LiC_6 primary particles and the surface is predominantly those of LiC_{12}.

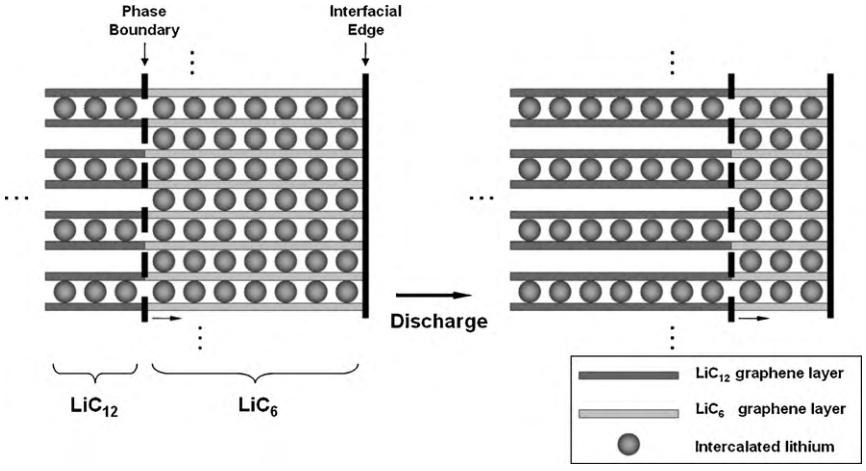

Fig. 8. Side view of the LiC_6-to-LiC_{12} phase transition in one dimension that occurs with in-plane movement of lithium [25] during discharge. The denoted phase boundary moves rightward as lithium is removed at the interfacial edge by electrochemical oxidation of the lithium intercalant. Removal of lithium can also occur *via* movement of intercalant from one interfacial edge to another.

would be complete when the planar phase boundaries reach the edge areas as depicted by the bottom stack in Fig. 7a and b depicts a secondary particle mid-way through discharge. In the fully charged state the particle might have been composed of LiC_6 stacks through and through. Electrochemical oxidation of lithium during discharge occurs at the interfacial-edge areas of stacks on the surface of the particle. Lithium in the lithium-rich LiC_6 stacks in the core region of the particle will move toward the particle surface resulting in the depicted radial variation in the two-phase stacks. After interruption of the discharge current and equilibration, the relative amounts of the two phases in all the stacks will be the same (see Fig. 19). In other words, the primary particles throughout the radii of the secondary particle will be of uniform composition after equilibration because in the simulations we allow movement of lithium between primary particles. In the model we take the exchange current density to be independent of the solid lithium composition because the outer edges of the stacks are the LiC_6 phase, at least in the early stages of discharge or charge.[9]

[9] In Fig. 19 we will show for the base case that after 20 s the stacks on the surface of the secondary particle are fully converted to LiC_{12}. Charge-transfer overvoltage is, however, not significant.

3.5. Heaviside mollification functions

The current during cell operation and the thermodynamic OCV of the lithiated graphite, in their most rigorous form, are step-change functions that typically cause numerical difficulties. We mitigate these potential problems by describing I and E_{ref}^{neg} as a heaviside mollification function, *flc2hs* in COMSOL, with parameters given in Table 4. The *flc2hs* function has two arguments corresponding to the 3rd and 4th table columns, "center" and "span," respectively; *flc2hs* is a smoothed, continuous switch function with a finite derivative. The function is zero for variable values less than "center" minus "span" and unity for values greater than "center" plus "span." For example the function for I (in A m^{-2}) for the case of the 40 s, 5C discharge pulse is $51.37 + 51.37 \times flc2hs((t - 40), 0.1)$; with *flc2hs*, I smoothly changes from a finite value to zero in a span of 100 ms. In Section 4.4 we also use *flc2hs* to investigate the effect of anisotropy in D_1^{pos}.

4. Results and discussion

Fig. 9 gives the experimental cell voltages during and after the charge and discharge pulses at 65% and 35% SOC. A certain degree of symmetry between the discharge and charge behavior

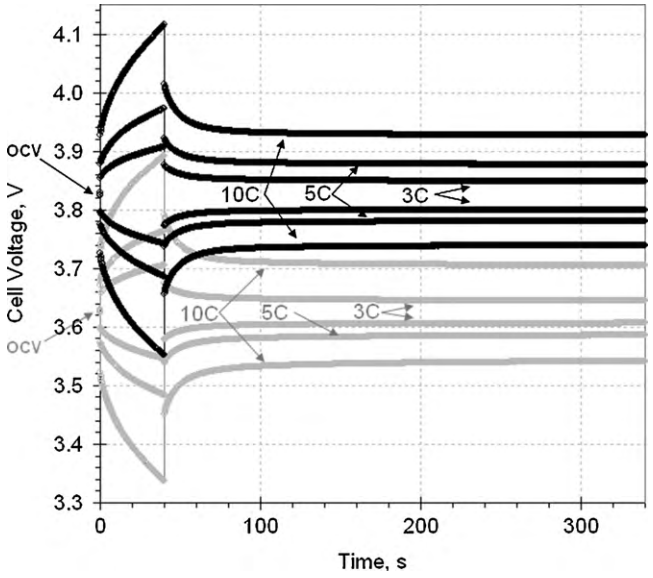

Fig. 9. Experimental cell voltage response to 3C, 5C and 10C current pulses. Black and grey symbols refer to 65% and 35% SOC, respectively. The OCVs prior to the pulses are designated on the ordinate. Data above and below OCV values correspond to charge and discharge data, respectively.

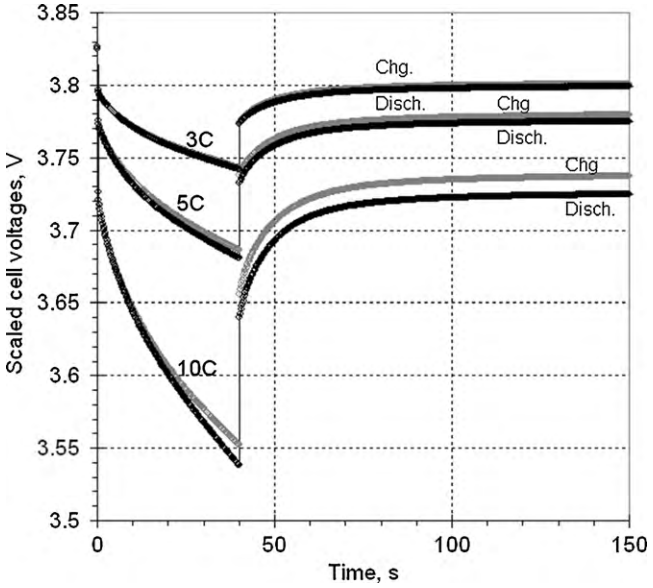

Fig. 10. Experimental cell discharge voltage (at 65% SOC) plotted with the charge data flipped to show symmetric behavior.

is immediately apparent. When the voltage of the first experimental data point (at 0.2 s) for either discharge or charge relative to the initial OCV is considered, we can see that this overvoltage at 5C is approximately half that at 10C, and that at 3C is about a third that at 10C: approximately 30, 50 and 100 mV were observed at 3C, 5C, and 10C, respectively, or both SOCs. Such a proportional relationship suggests that ohmic rather than charge-transfer processes control the cell behavior, at least initially. Typical saw-tooth polarization behavior is exhibited throughout the 40-s pulse. The relaxation of the overvoltage after current interruption appears to occur in two stages: rapid (<0.2 s) followed by a slower region with a timescale of about 150 s. Interestingly, not only does the same such proportional behavior of overvoltage to current exist for the rapid stage, the magnitudes are even comparable giving about 30, 50, and 100 mV of overvoltage relaxation in the first 0.2 s after current interruption. The slower overvoltage relaxation period is the same for charge and discharge and does not appear to be a strong function of current: relaxation to within 1 mV of the 5-min OCV at 65% SOC are observed within approximately 170, 210 and 220 s for the 3C, 5C, and 10C rates, respectively. Relaxation times at 35% SOC are about 10 s longer.

The symmetry between charge and discharge behavior is also demonstrated by Fig. 10. This figure shows the 65% SOC data from Fig. 9 with the charge data re-scaled to overlay the discharge data; for charge data at a given current, the first data point (at 0.2 s) was pinned to the corresponding first discharge data point and all charge polarization from that point were reversed in sign.

If the OCV *vs.* SOC function were linear, we would expect the voltages after 150 s to converge. A 40-s discharge pulse at the 10-C rate will cause an SOC change of 11%; a total "swing" in SOC of 22% is realized when one considers both charge and discharge pulses from a given SOC. In the range of the 22% SOC swing, the OCV *vs.* SOC function is hardly linear and would explain why the voltages after 150 s do not converge. The 3C data correspond to <7% SOC swing, which is small enough for linear behavior and thus the nearly exact overlay shown in Fig. 10.

4.1. Model/experiment comparisons of cell voltage behavior

Figs. 11 and 12 show the 65% SOC experimental results given in Fig. 9 along with model predictions using the base-case input data for discharge and charge, respectively. The value $D_1^{pos} = 1.4 \times 10^{-14}\ m^2\ s^{-1}$ gives the best fit between model and experimental results that is given in these figures and is well aligned with reported values [26]. These results are very sensitive to the value of D_1^{pos}. The reduction of D_1^{pos} by a factor of two, for example, results in significantly more polarization during the 10C pulse and a longer voltage relaxation period than is observed experimentally (see Fig. 17, which is discussed later). The overall satisfactory agreement shown suggests the validity of using a single D_1^{pos} for $y = 0.52 \pm 0.07$, which is the composition range investigated in this work. The 35% SOC experimental data are fit equally well with corresponding input data and a smaller value of $D_1^{pos} = 1.2 \times 10^{-14}\ m^2\ s^{-1}$. This results in slightly longer voltage-relaxation periods than at 65%. Dees et al. [26] also observed a decrease in diffusion coefficient at the same values of OCVs *vs.* Li/Li^+. For the sake of brevity, the 35% SOC model results are not shown.

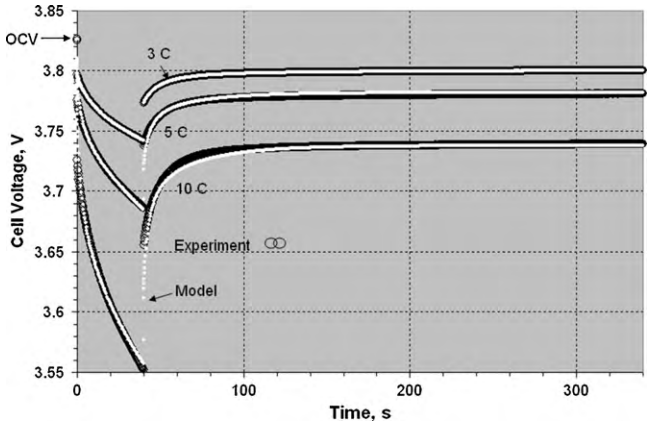

Fig. 11. Experimental 65% SOC discharge behavior from Fig. 9 (black open circles) plotted with results from simulations (white dots) for base-case conditions given in Tables 2 and 3.

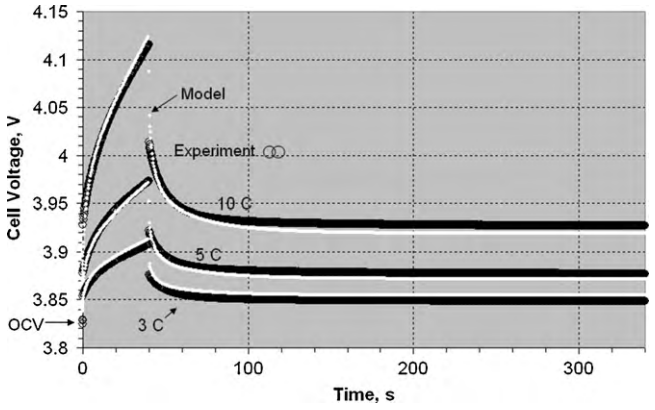

Fig. 12. Experimental 65% SOC charge behavior from Fig. 9 (black open circles) plotted with results from simulations (white dots) for base-case conditions given in Tables 2 and 3.

Discharge calculations showed better agreement with experiments than those of charge, especially for the final OCV. The experimental variation in initial OCV for the charge results shown in Fig. 12 that would indicate variation in experimental initial SOC, may partly be responsible for this 4–8 mV discrepancy. The OCVs prior to all the discharge pulses were within 0.5 mV of our characteristic OCV for 65% SOC (3.8264 V); OCVs prior to charge were within 3 mV.

4.2. Model calculations of cell overvoltage

Fig. 13 gives the V_{cell} model results for the 10C discharge pulse from 65% SOC and the thermodynamic OCV from the input data shown in Figs. 3 and 4. The data in Figs. 3 and 4 give the thermodynamic OCV of a cell, $E_{ref}^{pos}(y^0) - E_{ref}^{neg}(x^0) = E_{cell}(x^0, y^0)$, which would be at the equilibrated composition of the electrodes, that is, in the absence of concentration variations throughout the particles in the electrodes. Although this equilibrated state would perhaps be obtained after sufficient relaxation time in real experimental cells, the equilibrated compositions, x^0 and y^0, are calculated using Eqs. (21) and (22). The total cell overvoltage would be the difference between V_{cell} and E_{cell}. When we write the calculated cell voltage in terms of the model output

$$V_{cell} = \phi_1\big|_4 - \phi_1\big|_1 \tag{23}$$

the total cell overvoltage, $E_{cell} - V_{cell}$, can then be written as

$$\begin{aligned} E_{ref}^{pos}(y^0) - E_{ref}^{neg}(x^0) - V_{cell} = \; & -(\phi_1|_4 - \phi_1|_3) && \text{(a) solid ohmic positive} \\ & -\left(\phi_1\big|_3 - \phi_2\big|_3 - E_{ref}^{pos}\Big|_3\right) && \text{(b) charge-transfer positive} \\ & +\phi_2\big|_2 - \phi_2\big|_3 && \text{(c) liquid separator ohmic and concentration} \\ & +\left(\phi_1\big|_2 - \phi_2\big|_2 - E_{ref}^{neg}\Big|_2\right) && \text{(d) charge-transfer negative} \\ & -(\phi_1\big|_2 - \phi_1\big|_1) && \text{(e) solid ohmic negative} \\ & +E_{ref,eq}^{pos} - E_{ref}^{pos}\Big|_3 && \text{(f) solid concentration positive} \\ & +E_{ref}^{neg}\Big|_2 - E_{ref,eq}^{neg} && \text{(g) solid concentration negative} \end{aligned} \tag{24}$$

where the subscripts on the vertical lines refer to the boundaries defined earlier. In the above equation we have elected to write the total cell overvoltage in terms of eight contributions, (a) through (g).[10] In Fig. 13, and alternatively in Fig. 14, we depict the contributions to the total cell overvoltage and show that (a), (c), and (f) dominate. The contributors (d), (e), and (g) are associated with the negative electrode and together represent only a small portion of the cell overvoltage. The negative's relatively high electronic conductivity results in (e) being insignificant (<1 μV) for the duration of the pulse; contributions (d) and (g) are shown separately in Fig. 14 and do not exceed 10 mV. Contribution (g) presents itself after $t = 14$ s because at this point the surface of the particles at the separator interface of the negative have been fully converted to LiC_{12} (*i.e.*, $x = 0.5$). This will be discussed further in Section 4.5.

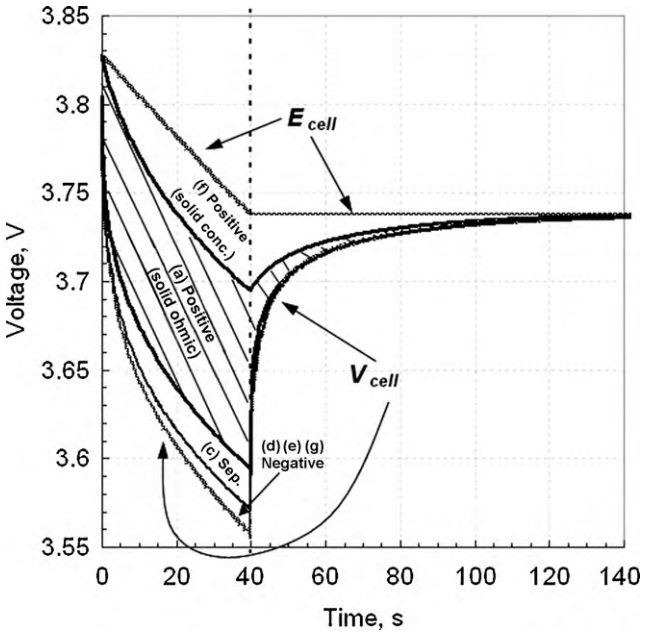

Fig. 13. Calculated contributions to the cell overvoltage during the 10-C discharge pulse given in Fig. 11. The calculated cell voltage (V_{cell}) and the thermodynamic OCV (E_{cell}) are indicated by the frayed line, and the overvoltage is between these lines. Areas indicating the overvoltage contributions are labeled with letters (a) through (f) corresponding to Eq. (24).

The three dominant contributors (a), (c), and (f) are present both before and after current interruption; however, (a) dominates before, and (f) dominates after. The magnitude of (a) can be attributed to the relatively low electronic conductivity in the positive. This term is non-zero when $I_{cell} = 0$ due to potential driving forces relating to the redox couples that are established within the positive relating to variations in y. This will be discussed in greater detail in the next section. The contribution due to (c) is best understood by looking at Eq. (2) and is due to an ohmic term, which is zero when $I_{cell} = 0$, and a concentration junction term [27] which is non-zero after current interruption. The dominant term after current interruption is (f) and is a direct reflection of reduced-lithium concentration variations throughout the particles in the positive electrode and is the subsequent subject of discussion.

[10] The way in which the contributions are defined is somewhat arbitrary; for example, we could have defined (b) at boundary 4 (instead of 3) and then (a) would be written in term of liquid-phase potential rather than solid.

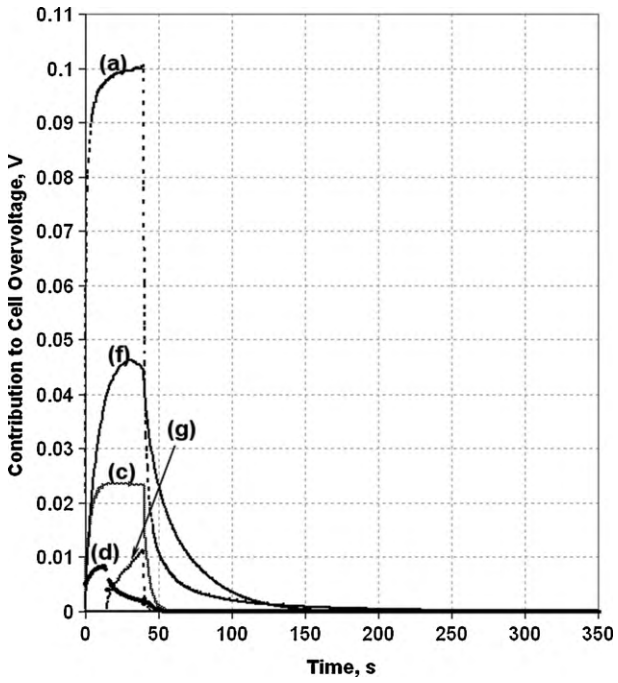

Fig. 14. Alternative representation of the overvoltage contributions given in Fig. 13. Data sets for the overvoltage contributions are labeled with letters (a) through (f) corresponding to Eq. (24). Contributions (b) and (e) are too small to be seen in this figure.

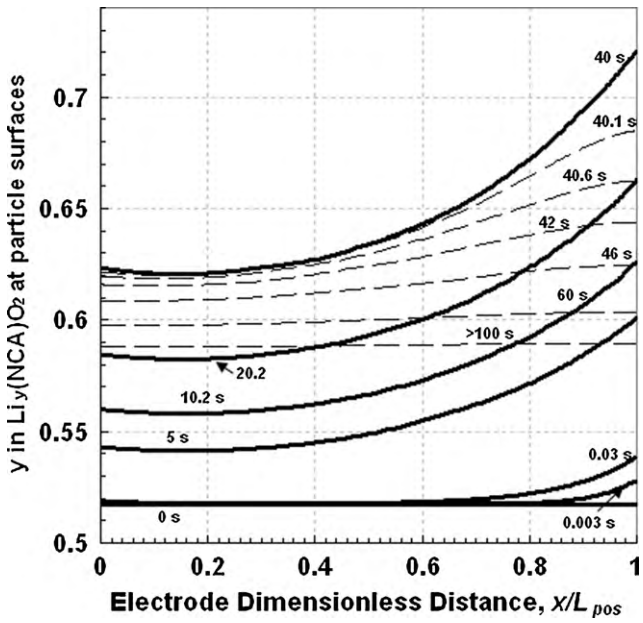

Fig. 16. Calculated lithium composition at the surface of the secondary particles as a function of particle position throughout the dimensionless positive-electrode half thickness. The results are for the 10-C discharge pulse followed by rest, and model input conditions are for the base case. The separator and current-collector interfaces are located at $x/L_{pos} = 0$ and 1, respectively. The solid lines correspond to profiles at times during the 40 s pulse, and the dashed lines correspond to those during the subsequent rest period.

4.3. Model calculations of Li in particles throughout the positive electrode

Fig. 15 gives calculations of lithium composition throughout a particle in the positive electrode at the current-collector interface for the 10-C discharge pulse. We have chosen to consider particles at the current collector boundary because the intercalation rate is initially highest at this location; this is because the effective conductivity of the solid phase is less than that of the liquid [28]; that is, $\kappa_1^{eff} < \kappa_2^{eff}$, which is frequently the case with the transition-metal oxide compounds used for positives in lithium-ion batteries. Prior to the pulse ($t = 0$) the composition throughout the particle is uniform at y = 0.52. Electrochemical reduction of solvated Li^+ then occurs at the solid/liquid interface ($y = 1$) upon initiation of the current pulse. Intercalation of the reduced-lithium species is apparent only very near the surface of the particle in the first 30 ms after current initiation. Intercalation reaches the core of the particle after 20 s; the particle surface reaches a maximum value of y = 0.72 just prior to current interruption ($t = 40$). One of the practical implications of this is that although 40-s discharge or charge pulses at the 10-C rate will result in an 11% change in cell SOC, the actual surface of the particles may experience up to a 32% change in SOC.

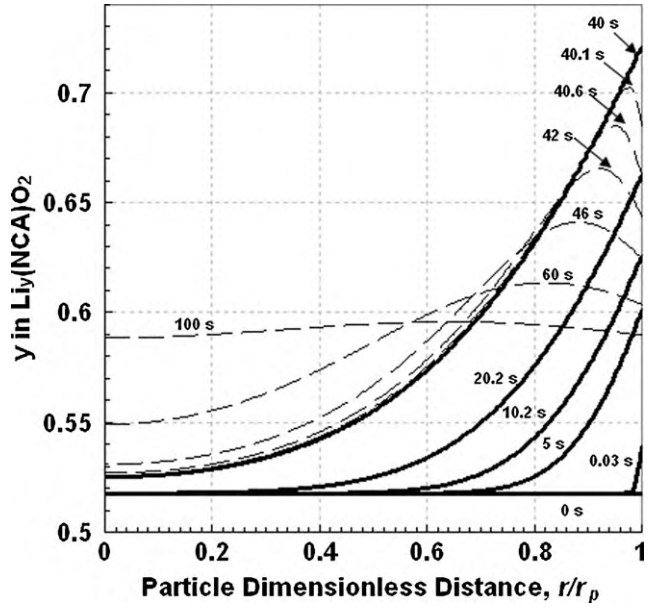

Fig. 15. Calculated lithium composition throughout a secondary particle in the positive electrode at the current-collector interface during the 10-C discharge pulse and rest for base-case model input conditions. The center and surface of the particle are located at $r/r_p = 0$ and 1, respectively. The solid lines correspond to profiles at times during the 40-s pulse, and the dashed lines correspond to those during the subsequent rest period.

The dashed lines in Fig. 15 show maxima in y *vs.* r/r_p after interruption. This behavior is an indication of oxidation of the intercalated Li at the particle surface during the rest period; that is, particles near the current collector are charged after current interruption and those near the separator are discharged. This internal galvanic coupling is responsible for the non-zero ohmic overvoltage for $40 < t < 150$ depicted in Figs. 13 and 14. This process also aids in the relaxation of y variations throughout the electrode, since particle-to-particle diffusion is not allowed by our treatment (only diffusion within the particles occurs).

Fig. 16 gives calculations of particle surface compositions throughout the cross section of the positive for the 10-C discharge pulse. As the initial conditions dictate, prior to the pulse the compositions throughout electrode are uniform at y = 0.52. In the instant after current initiation, the rate of intercalation is extremely non-uniform with the rate being highest at the current-collector interface ($x/L_{pos} = 1$). The 3-ms profile is evidence of this non-uniformity because it shows y > 0.52 only in the vicinity of the current collector. This is expected [28] initially (*i.e.*, within

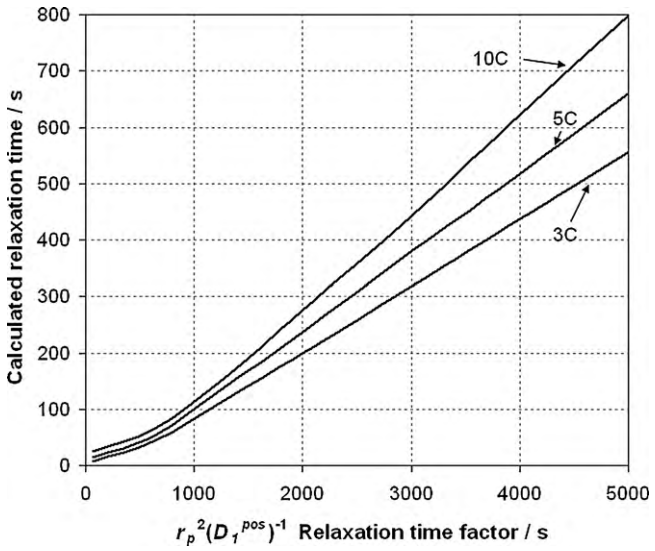

Fig. 17. Model calculations of relaxation time (for base-case input data) as a function of the relaxation time factor defined as $(r_p^{pos})^2/D_1^{pos}$ for the three different discharge current pulse magnitudes.

the first second) because $\kappa_1^{eff} < \kappa_2^{eff}$ and results in the 60–80 mV ohmic contribution to the overvoltage seen in Fig. 14. We then see that this ohmic contribution is larger for the remainder of the pulse because intercalation is now occurring at all values of x, which indicates an even larger portion of current flowing in the resistive solid phase than initially (relative to that in the liquid). In fact, the characteristic shape exhibited by the 5, 10, 20, and 40-s profiles shown in Fig. 16 is because after about 1 s the intercalation rate is nearly uniform in both x and t. During the relaxation period the composition of the particles approach uniformity in x (and r) *via* the internal galvanic coupling described above.

Fig. 17 shows the relationship between the calculated relaxation time (for base-case input data) and the value of a relaxation time factor defined as $(r_p^{pos})^2/D_1^{pos}$ for the three different 40 s discharge current pulse magnitudes. We define the relaxation time to be the minimum time after current interrupt for which the percent variation between the maximum and minimum value of y in r for all the particles is less than $1.20 \pm 0.02\%$. For values of relaxation times greater than about 50 s, the relationship is clearly linear, owing to the dominance of (f) over other processes (see Fig. 13); that is, if (a), (b), or (c) dominated, then such a relationship would not be observed. Of course, for the case of single-particle relaxation without charge transfer, the relationship would also be linear (and pass through the origin).

The cases with relaxation times of about 50 s and lower are associated with small variations of "y" throughout the particles and approach the behavior of a 1-dimensional (in x) electrode with $(r_p^{pos})^2/D_1^{pos} \rightarrow 0$. With no resistance to Li diffusion in the particles, Li composition variations would still exist throughout the electrodes due to the very non-uniform charge-transfer reaction rate distribution in x (see Fig. 16) and relaxation time would show less dependence on the $(r_p^{pos})^2/D_1^{pos}$ factor. This explains the finite value of the ordinate intercept and the corresponding non-linear behavior for relaxation times less than 50 s.

Also note that for each value of the relaxation time factor, data were generated for four values of r_p^{pos} (2.5, 3, 4, and 6 μm and associated values of D_1^{pos}) and resulted in the same relaxation time. This would not be the case if κ_1^{eff} were a strong function of r_p.

4.4. Investigation of anisotropic Li diffusivity in the positive particles

Fig. 18 shows typical calculated and experimental cell voltage response within the first 3 s after the onset of a 10C discharge pulse. One can see up to a 25 mV discrepancy between the model (for the case of $D_1^{pos} = 1 \times 10^{-13}$ m^2 s^{-1}) and experiment due to the slower polarization rate of the model results. A similar effect is observed on current interrupt in that the calculations show a slower rate of depolarization in the first few seconds after current interrupt. The calculation with a 20-fold decrease in D_1^{pos}, also shown in the figure, exhibits more rapid polarization in the first 200 ms, however, agreement between model and experiment is sacrificed thereafter. This effect could be explained by the periphery of the positive particles being more resistive to Li diffusion than the bulk. To investigate this we invoked an anisotropic D_1^{pos} with behavior indicated in the inset of the figure (see Table 4 for heaviside function parameters of D_1^{pos}). In the anisotropic case, the bulk of the particle has $D_1^{pos} = 2 \times 10^{-13}$ with a thin layer having $D_1^{pos} = 5 \times 10^{-17}$.[11] The anisotropic case indicates initially more rapid polarization and does not sacrifice agreement at longer times. This result indicates that the primary particles on the periphery of the secondary particles (in contact with the electrolytic solution) may be more resistive to diffusion of reduced Li than those in the bulk. Also, removal (or mitigation through particle coatings) of the resistive layer would have the effect of doubling D_1^{pos}.

4.5. Model calculations of Li in particles throughout the negative electrode

For the 10-C discharge pulse, Fig. 19 gives calculated average lithium composition throughout a secondary particle at the separator interface of the negative and Fig. 20 gives particle surface compositions throughout the electrode cross section. Prior to the pulse ($t = 0$) the composition throughout the particle is uniform at x = 0.77. Since Fig. 3 indicates that two-phase equilibrium exists at this value of "x," one can look at the right ordinate axis of this figure and see that at 65% SOC, the negative consists of about 55% LiC_6 and 45% LiC_{12}. Our assumption that this value of "x" exists throughout the electrode uniformly prior to the pulse (see Fig. 20) may be appropriate because we set the SOC in the experimental cell with a relatively low discharge rate (1C). Oxidation of the Li in the LiC_6 phase of the primary particles located on the surface of the secondary particles (see Fig. 7) results in solvated Li^+ in the liquid phase[12] and commences with the onset of the current pulse. In contrast to the positive, $\kappa_1^{eff} > \kappa_2^{eff}$ for the negative electrode; because of this we see initially de-intercalation predominantly in the particles adjacent to the separator [28]. In fact Fig. 19, which represents particles adjacent to the separator, shows that de-intercalation is at first apparent only at the surface of these particle (see the 0.03 and 5-s profiles). Within the first 14.2 s of the pulse, only contribution (d), charge-transfer overvoltage, which mirrors the behavior of ϕ_2, is apparent in Fig. 14.

At $t = 14.2$ (see also Fig. 20) primary particles at the surface of the secondary particles located at the separator are fully converted to LiC_{12} (x = 0.5) and $E_{ref}^{neg}(x)$ is no longer constant at 85 mV. Near the step change at x = 0.5, very small increases in "x" would result in large increases in $E_{ref}^{neg}(x)$, which would make further de-intercalation at this point less favorable; de-intercalation therefore

[11] Specifically, $D_1^{pos} = 1.90000 \times 10^{-13} - 1.89955 \times 10^{-13} \times flc2hs((y - 0.994), 0.002)$.

[12] The Li^+ species formed by the charge-transfer reaction occurring at the particle surface is in actuality transported through the SEI prior to reaching the liquid phase where solvation would occur.

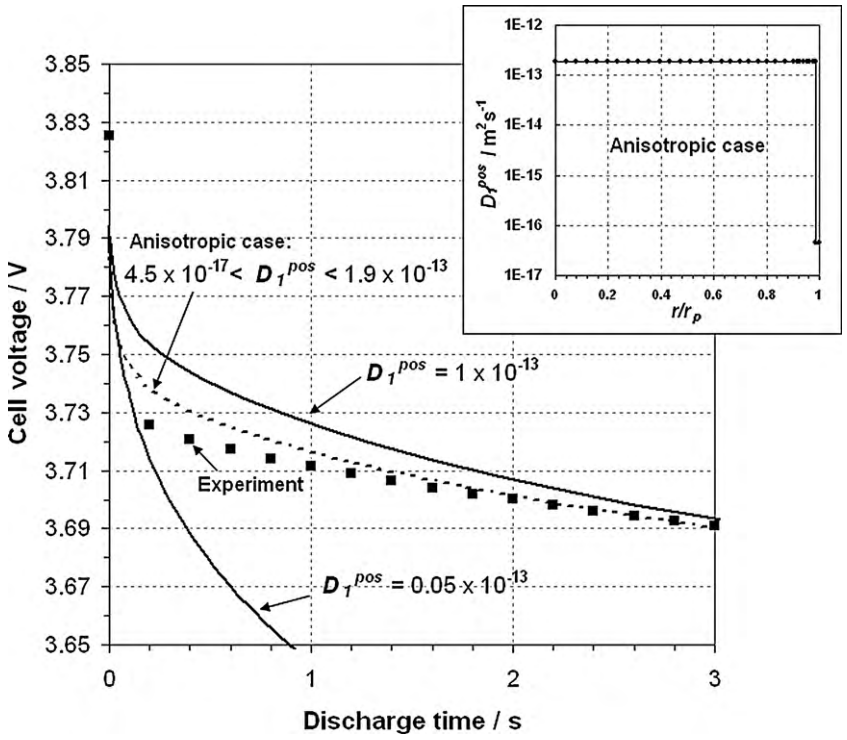

Fig. 18. Initial cell voltage behavior for 10C current pulses. Dashed and solid lines, respectively, are model calculations for anisotropic and isotropic D_1^{pos} in $m^2\ s^{-1}$; points represent experimental results. The inset shows the variation of D_1^{pos} throughout the particles for the anisotropic case in which D_1^{pos} varies from 4.5×10^{-17} near the particle periphery to 1.9×10^{-13} in the bulk of the particle (see Table 4 for heaviside function parameters).

becomes more preferable deeper into the electrode (in the direction toward the current collector) than at the separator. Because of this, we see that at the separator the particle surface remains at x = 0.5 for the duration of the pulse and does not fall below this value (which would indicate formation of LiC_{18}). The 20.2 and 40-s profiles given in Fig. 20 show that the surface of the particles located at $x/L_{neg} = 0.94$ and 0.76, respectively, have the same experience that the particles at the separator had at $t = 14.2$ s. All this gives the appearance of a reaction "front" that is formed at $t = 14.2$ s and moves deeper and deeper in to the electrode toward the current collector until the current is interrupted at $t = 40$ s. A longer pulse at this rate would allow the reaction front to reach the current collector and exhaust all the LiC_6 on the surface of the secondary particles. A value of $\phi_1 - \phi_2 - 0.085 > 35$ mV anywhere within the negative

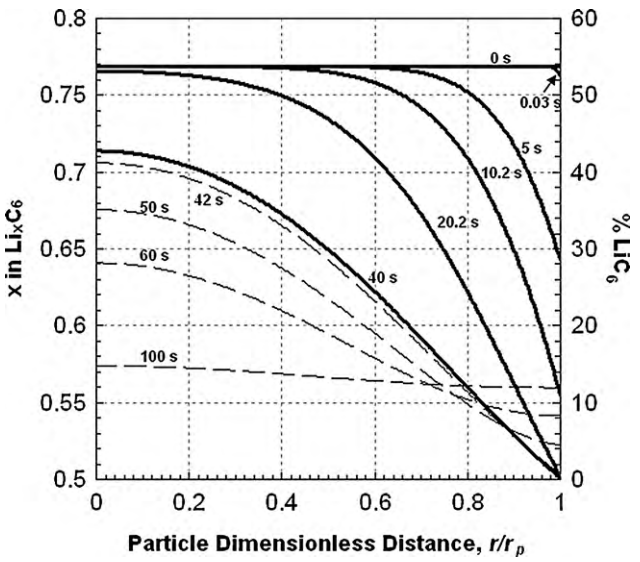

Fig. 19. Calculated average lithium composition throughout a secondary particle in the negative electrode residing at the separator interface during the 10-C discharge pulse and rest for base-case model input conditions. The center and surface of the particle are at $r/r_p = 0$ and 1, respectively. The alternate ordinate gives the percent LiC_6, the balance being LiC_{12}. The solid lines correspond to profiles at times during the 40-s pulse, and the dashed lines correspond to those during the subsequent rest period.

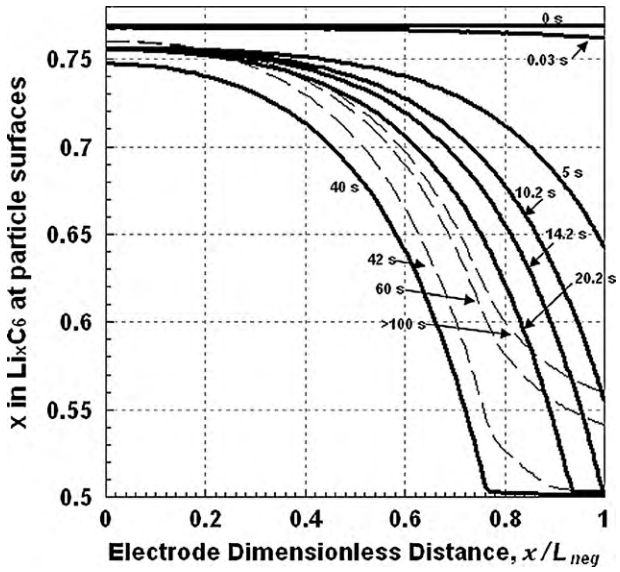

Fig. 20. Calculated average lithium composition at the surface of the secondary particles as a function of particle position throughout the dimensionless negative electrode half thickness. The current-collector and separator interfaces are located at $x/L_{pos} = 0$ and 1, respectively. The results are for the 10-C discharge pulse followed by rest, and model input conditions are for the base case. The solid lines correspond to profiles at times during the 40-s pulse, and the dashed lines correspond to those during the subsequent rest period.

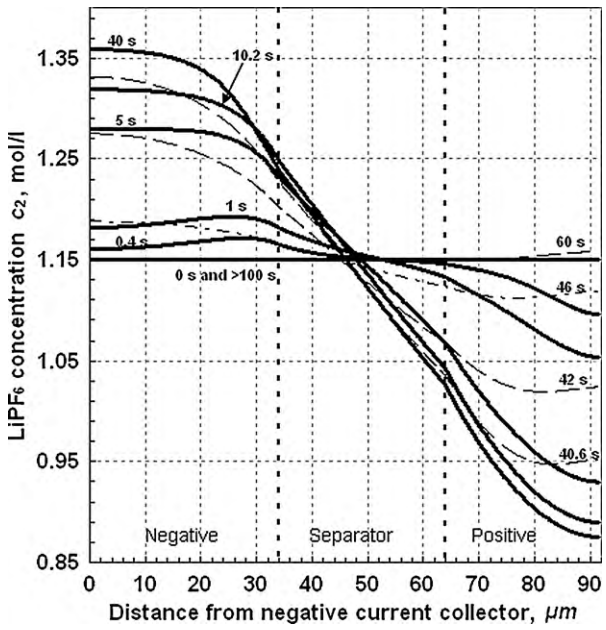

Fig. 21. Model calculations of $LiPF_6$ concentation in the liquid-filled pores throughout the unit cell for the 10C discharge pulse and base-case input conditions. The solid lines correspond to profiles at times during the 40-s pulse, and the dashed lines correspond to those during the subsequent rest period.

electrode will allow "x" to decrease below 0.5 (indicating formation of LiC_{18}); the value does not exceed 10 mV for the magnitude and duration of the pulses that we have considered and therefore LiC_{12} is the only delithiated phase that we predict. A higher pulse current of the same duration would also cause $\phi_1 - \phi_2 - 0.085 > 35$ mV and result in LiC_{18} formation.

Contribution (g), the concentration overvoltage, is apparent as $x \rightarrow 0.5$ (after $t = 14.2$ s) as indicated in Fig. 14. The behavior of (g) is determined by the variable span for the E_{ref}^{neg} heaviside function (see Table 4); that is, the heaviside function allows E_{ref}^{neg} to rise above 0.085 V slightly before $x = 0.5$ and this results in the (g) values shown. There would not be values of (g) between 0 and 35 mV with a perfect step function. A look at the sum of (d) and (g) is perhaps more useful because it represents charge-transfer overvoltage based only on the 85-mV plateau and removes the effects of the heaviside function.

After current interruption, the model predicts the redistribution of the LiC_{12} and LiC_6 phases primarily via diffusion between the primary particles. During relaxation Fig. 20 shows that the surfaces of the secondary particles near the separator are not pure LiC_{12} (as they were during the pulse after 14 s), rather they are a mix of LiC_6 and LiC_{12}. In contrast to the positive, the relaxed profile is not a uniform "x" value because of the two-phase nature of lithiated graphite in this composition range. Galvanic coupling as a driving force to equalize "x" does not present itself in the negative because the system rests on a voltage plateau; after complete relaxation, the particles at the current collector have a nearly equal mole ratio of LiC_6 to LiC_{12} and those at the separator are about 90% LiC_{12} (see Fig. 19).

4.6. Model calculations of liquid $LiPF_6$ concentration throughout the cell

Fig. 21 gives the calculations of c_2 in the liquid-filled pores throughout the cell sandwich for the 10C discharge pulse. Within the first 12 s of the pulse, a pseudo-steady state profile is established that remains relatively unchanged until current interruption. Contribution (c) in Fig. 14 ($\Delta\phi_2$ across the separator) coincides with this by showing a leveling to about 24 mV after 12 s. The concentration c_2 then relaxes to nearly uniform concentration in about the same time period after the interrupt; again coinciding with the behavior of (c) which is determined by the liquid junction potential [27]. During the pulse, contribution (c) is composed of both an ohmic portion as well as a liquid junction potential. The small consequence to the cell overvoltage (<12 mV) of this liquid junction throughout the separator is seen at the point of current interruption in Fig. 14. At current interruption the ohmic portion of (c) is removed and only the liquid concentration-junction potential remains. Although the overvoltage associated with the liquid electrolytic solution is relatively small for the conditions of this study, Fig. 2 suggests that pulses at lower temperature would result in substantially larger overvoltages.

5. Conclusions

In this work we demonstrate how to utilize the predictive capabilities of lithium-ion battery modeling. Predictions of cell voltage during charge and discharge current pulses and subsequent relaxation show good agreement with experimental results. We have identify the major contributions to cell overvoltage during pulse current conditions that would be encountered in HEV operation. The ohmic voltage loss of the solid positive active material is by far the dominant contributor in the first instances of a pulse. The concentration overvoltage associated with the reduced lithium in the solid phase of the positive is initially non-existent and of secondary importance through pulse duration; however, it dominates voltage response after current interruption. Calculations show that for relaxations times greater than about 50 s, relaxation time varies linearly with the positive's particle radius squared over the diffusion coefficient. A diffusion coefficient of about 1×10^{-14} m^2 s^{-1} fit our experimental results and is well aligned with reported values for the positive material studied [26].

In the model we utilize heaviside-type functions to describe the multiple two-phase and single-phase regions of the thermodynamic OCV of lithiated graphite. We have extended the "pleated-layer model" to realize the behavior of the primary-particle aggregates (*i.e.*, secondary particles) during cell operation. Although the negative contributes little to the cell overvoltage, the two-phase behavior results in a reaction front of a particular phase composition on the surface of the particles within the electrode that moves deeper and deeper into the electrode until a current pulse is interrupted. Such a reaction front would not be observed in modeling studies that did not account for the true thermodynamic behavior of graphite. Those studying stress cracking of particles should be aware of this behavior. Study of the ohmic and charge-transfer overvoltage behavior of the negative would likely require low-temperature testing with a reference electrode.

In contrast to the positive which exhibits significant voltage relaxation after a current pulse, the negative shows no voltage relaxation because of the two-phase nature in the region we investigated. After full relaxation, a stable composition gradient of lithium exists throughout the solid phase of the negative. After relaxation of the positive, no such composition gradients exist because they are removed by internal galvanic coupling. We investigate the effect of an anisotropic Li diffusion coefficient in the positive particles on the predicted cell voltage behavior and find better agreement between model and experimental results in the first instances of the pulse. The results are consistent with the periphery of the particle being more resistive to diffusion of reduced Li than the bulk. Mitigation of this could significantly increase cell voltage during current pulse operation and result in increased fuel economy in HEV applications.

Calculations of the lithium concentration throughout the particles indicate that the surface of the particles may experience a much larger SOC change than the overall cell SOC change. High rate pulses at low and high cell SOC should be carefully considered in HEV operation. If, for example, repeated formation of de-lithiated positive-electrode material leads to degradation in particle structural integrity, then high-rate charge pulses at high SOC should be controlled. Conversely, if repeated formation of the highly de-lithiated graphite phases (*e.g.*, LiC_{36}) results in degradation, then high-rate discharge pulses at low SOC should be limited. Such information should be taken into account in the design of vehicular battery control modules.

Acknowledgements

Our thanks go to many at SB LiMotive that were involved in this work; we especially thank those assisting in the cell construction, cell testing, and measurements of liquid-phase conductivity. We also express our gratitude to Rajeswari Chandrasekaran for her help and in particular for obtaining reference-electrode measurements and fitting coefficients for the conductivity expression. Thanks also go to Ted Miller and Kent Snyder of Ford Motor Company for their support.

References

[1] T.F. Fuller, M. Doyle, J. Newman, J. Electrochem. Soc. 141 (1) (1994) 1–10.
[2] S. Santhanagopalan 1, Q. Guo, P. Ramadass, R.E. White, J. Power Sources 156 (2006) 620–628.
[3] T.F. Fuller, M. Doyle, J. Newman, J. Electrochem. Soc. 141 (4) (1994) 982–990.
[4] P. Arora, M. Doyle, A.S. Gozdz, R.E. White, J. Newman, J. Power Sources 88 (2000) 219–231.
[5] M. Doyle, Y. Fuentes, J. Electrochem. Soc. 150 (6) (2003) A706–A713.
[6] K. Kumaresan, G. Sikha, R.E. White, J. Electrochem. Soc. 155 (2) (2008) A164–A171.
[7] I.J. Ong, J. Newman, J. Electrochem. Soc. 146 (12) (1999) 4360–4365.
[8] K. Smith, C.-Y. Wang, J. Power Sources 161 (2006) 628–639.
[9] W.F. Fang, O.J. Kwon, C.Y. Wang, Y. Ishikawa, SAE 2009, 2009-01-1388 (2009).
[10] H. Horie, T. Abe, T. Kinoshita, Y. Shimoida, Presented at the EVS23 Electric Vehicle Symposium, Anaheim Convention Center, December 2, 2007.
[11] P. Albertus, J. Christensen, J. Newman, J. Electrochem. Soc. 156 (7) (2009) A606–A618.
[12] D. Dees, E. Gunen, D. Abraham, A. Jansen, J. Prakash, J. Electrochem. Soc. 155 (8) (2008) A603–A613.
[13] COMSOL Multiphysics®, Chemical Engineering Module – User's Guide, Version 3.4, October, 2007.
[14] COMSOL Multiphysics®, Chemical Engineering Module – Model Library, Version 3.5a "Rechargeable Li-Ion Battery," November, 2008, pp. 717–741.
[15] M. Doyle, J. Newman, A.S. Gozdz, C.N. Schmutz, J.-M. Tarascon, J. Electrochem. Soc. 141 (1) (1994) 1890–1903.
[16] M. Doyle, T.F. Fuller, J. Newman, J. Electrochem. Soc. 140 (6) (1993) 1526–1553.
[17] L. Valøena, J.N. Reimersa, J. Electrochem. Soc. 152 (5) (2005) A882–A891.
[18] T. Ohzuku, Y. Iwakoshi, K. Sawai, J. Electrochem. Soc. 140 (9) (1993) 2490–2498.
[19] D.A.G. Bruggemann, Ann. Phys. 24 (1935) 636–679.
[20] M.W. Verbrugge, B.J. Koch, J. Electrochem. Soc. 141 (11) (1994) 3053–3059.
[21] M.W. Verbrugge, B.J. Koch, J. Electrochem. Soc. 146 (3) (1999) 833–839.
[22] M.W. Verbrugge, B.J. Koch, J. Electrochem. Soc. 143 (1996) 600–608.
[23] E. Peled, J. Electrochem. Soc. 126 (12) (1979) 2047–2051.
[24] K. Edström, M. Herstedt, D. Abraham, J. Power Sources 153 (2006) 380–384.
[25] M.S. Dresselhaus, G. Dresselhaus, Adv. Phys. 51 (1) (2002) 1–186.
[26] D.W. Dees, S. Kawauchi, D.P. Abraham, J. Prakash, J. Power Sources 189 (2009) 263–268.
[27] J. Newman, Electrochemical Systems, 2nd ed., Prentice Hall, Englewood Cliffs, NJ, 1991.
[28] J. Newman, W. Tiedemann, AIChE J. 21 (1975) 25–41.
[29] Y.-H. Chen, C.-W. Wang, G. Liu, X.-Y. Song, V.S. Battaglia, A.M. Sastry, J. Electrochem. Soc. 154 (10) (2007) A978–A986.